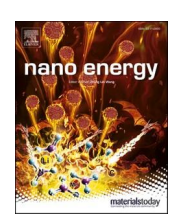


Contents lists available at ScienceDirect

Nano Energy

journal homepage: www.elsevier.com/locate/nanoen





Engineering the architecture and oxygen deficiency of T-Nb₂O₅-carbon-graphene composite for high-rate lithium-ion batteries

Panpan Jing ^{a,b}, Kuanting Liu ^c, Luke Soule ^a, Jenghan Wang ^c, Tongtong Li ^a, Bote Zhao ^{a,*}, Meilin Liu ^{a,*}

- ^a School of Materials Science and Engineering, Georgia Institute of Technology, Atlanta, GA 30332, USA
- b School of Materials Science and Engineering, Shaanxi Key Laboratory of Green Preparation and Functionalization for Inorganic Materials, Shaanxi University of Science & Technology, Xi'an, Shaanxi Province 710021. China
- ^c Department of Chemistry, National Taiwan Normal University, Taipei 116, Taiwan

ARTICLE INFO

Keywords: Lithium-ion battery High-rate capability $T\text{-Nb}_2\text{O}_5$ 2D architecture Oxygen deficiency

ABSTRACT

Developing advanced architectures using a cost-effective synthesis strategy is still a challenge for wide-spread commercial application of Nb₂O₅ in high-power rechargeable lithium-ion batteries (LIBs). Here we report a new two-dimensional (2D) architecture composed of oxygen-vacancy-rich T-Nb₂O₅ on reduced graphene oxide nanosheet and carbon (2D Nb₂O₅-C-rGO), which is synthesized via a one-pot hydrolysis route followed by a heattreatment. As an anode for LIBs, the 2D Nb₂O₅-C-rGO architecture shows excellent rate capability (achieving a capacity of 114 mAh g⁻¹ at 100 C or 20 A g⁻¹) and cycling stability (maintaining a capacity of 147 mAh g⁻¹ at 5 C for 1,500 cycles and 107 mAh g⁻¹ at 50 C for 5,000 cycles). Experimental investigations and density functional theory (DFT)-based calculations reveal that the outstanding Li⁺ storage performance of the 2D Nb₂O₅-C-rGO electrode is attributed to the enhanced electronic conductivity facilitated by the C-rGO electronic network and fast Li⁺ migration within small Nb₂O₅ grains enhanced by in-situ formed lattice oxygen vacancies, which alter the Nb d band structure and Li⁺ interaction. This work results in an anode with advanced architecture for fast Li⁺ storage and provides more insight into the energy storage mechanism in the Nb₂O₅-based carbonaceous composite electrodes.

1. Introduction

Due to the huge market prospects and rapid evolutions on the hybrid/plug-in/pure electric vehicles, the fast-rechargeable LIBs are in the accelerated development now [1,2]. As an indispensable reversible electrochemical energy storage device, LIBs face many scientific and technical challenges for the emerging applications. For example, one of the most severe bottlenecks to the technology is to design a suitable anode material with high-rate capability, long-term stability, and high-safety [3,4]. Starting with graphite at the earliest, hundreds of materials have been developed as the anodes for LIBs to date, which into three main groups, classified could including intercalation/de-intercalation materials (such as graphite [5,6], TiO₂ [7], $\text{Li}_4\text{Ti}_5\text{O}_{12}$ [8], Nb_2O_5 [9], LiNbO_3 [10], $\text{Ti}_2\text{Nb}_{2x}\text{O}_{4+5x}$ [11] and Nb₁₆W₅O₉₃ [12]), alloy/de-alloy materials (such as Si, Ge and P) [13-15], and conversion materials (such as Co₃O₄, WS₂ and MoSe₂) [16-18]. Among those materials, niobium pentoxides (Nb₂O₅) are considered a very promising intercalation-type anode candidate because of its desirable working potential (above 1.0 V vs. Li/Li⁺) for high safety (minimal reaction with most liquid electrolytes and avoiding lithium dendrite growth and solid-electrolyte-interphase formation), considerable theoretical capacity (from 200 to \sim 400 mAh g⁻¹), and fast cycling rates enabled by the open framework with small volume change (less than 5%) during cycling [9,19-24]. These unique properties make $\mathrm{Nb_2O_5}$ more attractive for high power batteries than graphite (theoretical capacity: 372 mAh g⁻¹; working potential: <0.2 V vs Li⁺/Li) and $\text{Li}_4\text{Ti}_5\text{O}_{12}$ (175 mAh g⁻¹; working potential: >1 V vs. Li^+/Li) [22,24,25]. Under carefully controlled conditions, Nb₂O₅ can crystalize in different structures, including the T-phase (orthorhombic), TT-phase (disordered T-phase), H-phase (monoclinic) and M-phase (tetragonal) [9,19,21,23, 26]. Although recent studies suggest that the H- and M-phase can deliver a relatively high capacity at low cycling rates [23,26], the *T*-phase is still the mostly studied one so far because the layered crystal structure allows fast Li⁺ diffusion and high rate-capability. However, its reversible Li⁺

* Corresponding authors.

E-mail addresses: bote.zhao@mse.gatech.edu (B. Zhao), meilin.liu@mse.gatech.edu (M. Liu).

storage capacity and rate-performance are still inadequate for many emerging applications, due largely to insufficient electronic and ionic conductivities [25,27,28].

To address these issues, which also exist in other oxide materials systems, the most commonly strategies is to design nanostructures with integrating carbonaceous materials and active materials. These strategies can reduce the diffusion distances of Li⁺/electrons and enhance the electronic conductivity of the active materials simultaneously. To date, a lot of progress have been achieved on improving the Li+ storage performance of T-Nb₂O₅, such as designing a 3D holey-graphene/Nb₂O₅ composite [28] and a carbon-encapsulated Nb₂O₅ nanocrystal [29]. Although such achievements of those techniques leveraged a hydrothermal or solvothermal processes followed by a annealing in inert atmospheres are very impressive, they are notoriously difficult to scale up because of the precise parameter controls. Moreover, the lattice oxygen vacancy could be created when the active materials obtained via a heat-treatment in an inert or reducing environment [7,30-32]. A certain amount of oxygen vacancy would affect the bulk electronic and ionic conductivities of an electrode material [7,30–32]. Therefore, the oxygen vacancy could also make a non-negligible contribution to those reported Nb₂O₅/carbonaceous composites even though the contribution was not considered [25,28,29].

Based on the above considerations, we have designed and synthe-sized a new 2D Nb₂O₅-C-rGO architecture using a facile and scalable hydrolysis route followed by a heat-treatment in Ar. The obtained 2D Nb₂O₅-C-rGO architecture displayed outstanding rate capability and cycling stability as an anode material for fast-rechargeable LIBs due largely to the efficient C-rGO conductive network, the in-situ formed lattice oxygen vacancies, and the restricted Nb₂O₅ grain size, as confirmed by experimental measurements and theoretical calculations.

2. Results and discussion

Fig. 1 schematically illustrates the two critical steps in the synthesis of the 2D Nb₂O₅-C-rGO architecture. Firstly, Nb⁵⁺ ions in the precursor

solution (Fig. 1a) were hydrolyzed into Nb(OH) $_5$ and DA monomers were self-polymerized into PDA with assistance of NH $_4$ ·H $_2$ O. Meanwhile, a Nb(OH) $_5$ -PDA composite was formed around the GO nanosheets with tens of micrometers in size (Fig. S1), as shown in Fig. 1b. Regarding the as-formed Nb(OH) $_5$ nucleus, some were spontaneously inserted into the PDA matrix while others were anchored on the near-surface of the PDA matrix. Secondly, the composite precursor was freeze-dried and annealed in Ar at 800 C for 2 h to form the 2D Nb $_2$ O $_5$ -C-rGO architecture (Fig. 1c). The as-formed carbon, derived from PDA, in the composite electrode could potentially enhance the electron transport between the Nb $_2$ O $_5$ and rGO, denoted as "bridge-C".

The microscopic features of the 2D Nb₂O₅-C-rGO architecture were characterized by using field-emission scanning electron microscopy (FE-SEM) and aberration-corrected scanning transmission electron microscopy (STEM). As shown in Figs. 2a and S2a, curved sheet structures are observed with abundant nanoparticles tightly and individually anchored on the surface of the sheet. The average size of the nanoparticles is ~34 nm (Fig. S2e). For a direct comparison, the SEM images of the controlled samples, including Nb₂O₅-rGO composite, Nb₂O₅-C composite, and pure Nb₂O₅, are also presented in the same fashion (Fig. S2b-d). The Nb₂O₅-rGO composite (Fig. S2b and inset) also has a 2D sheet-like morphology, similar to that of the Nb₂O₅-C-rGO architecture. Although those nanoparticles are still relatively dispersed, their sizes are much larger (with an average of 87 nm) than that of the 2D Nb₂O₅-CrGO architecture. The morphology of the Nb₂O₅ in the Nb₂O₅-C composite is nanoparticle with average size of 57 nm (Fig. S2c). Without the assistance of bridge-C and rGO, the pure Nb2O5 (Fig. S2d) has much larger particle size (average: 146 nm) (Fig. S2f).

Fig. 2b–d shows the STEM images of the 2D Nb₂O₅-C-rGO architecture, in which the components of Nb₂O₅ particles, bridge-C, and rGO can be distinguished. The bridge-C appears to be amorphous and the rGO has a typical multi-layer nanosheet morphology. In terms of the Nb₂O₅ nanoparticles marked as "1" and "2" in Fig. 2c, some are inserted into the C matrix while some marked as "2" appear to be coated with the thin C layer and anchored on the surface of the C matrix. Through

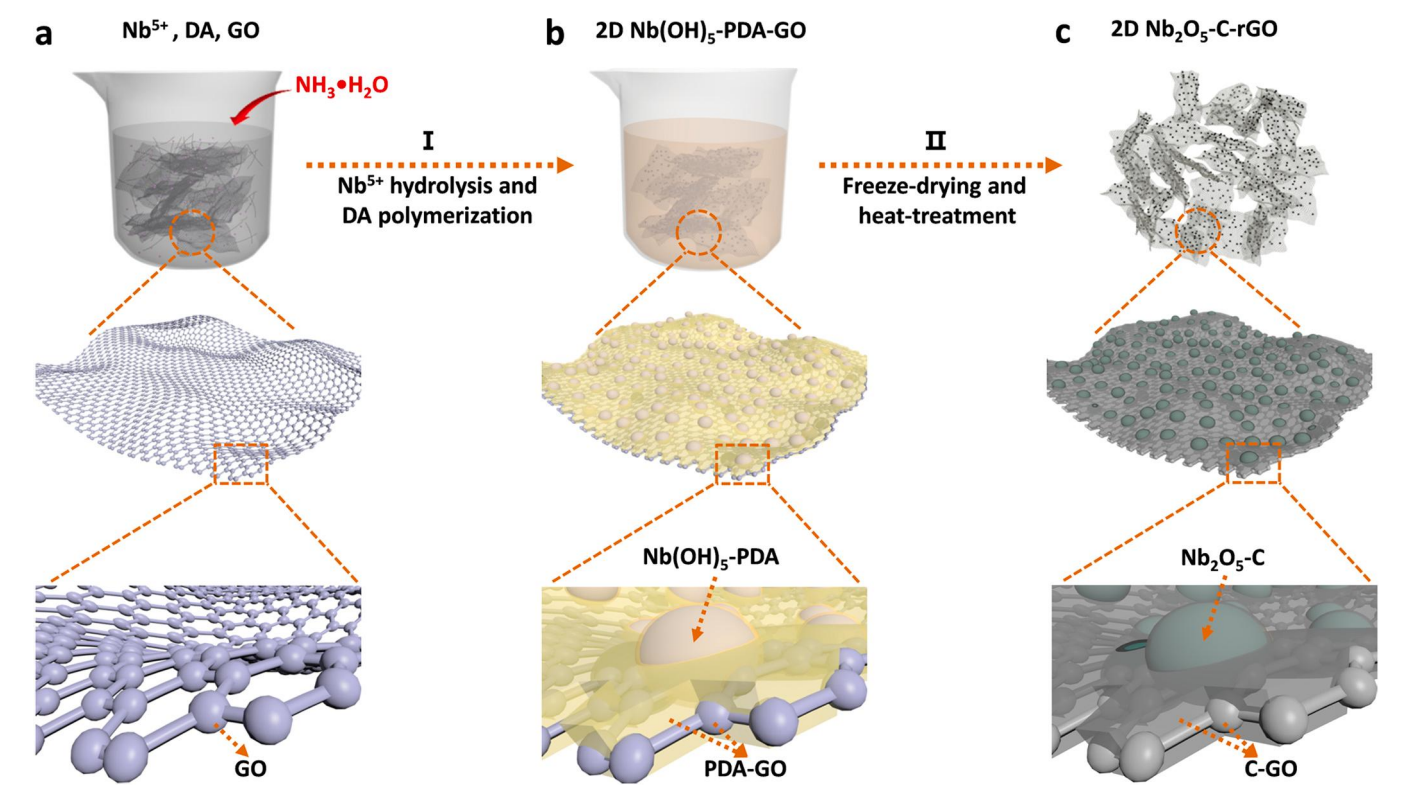


Fig. 1. Schematic illustration of synthesis procedure of the 2D Nb₂O₅-C-rGO architecture.

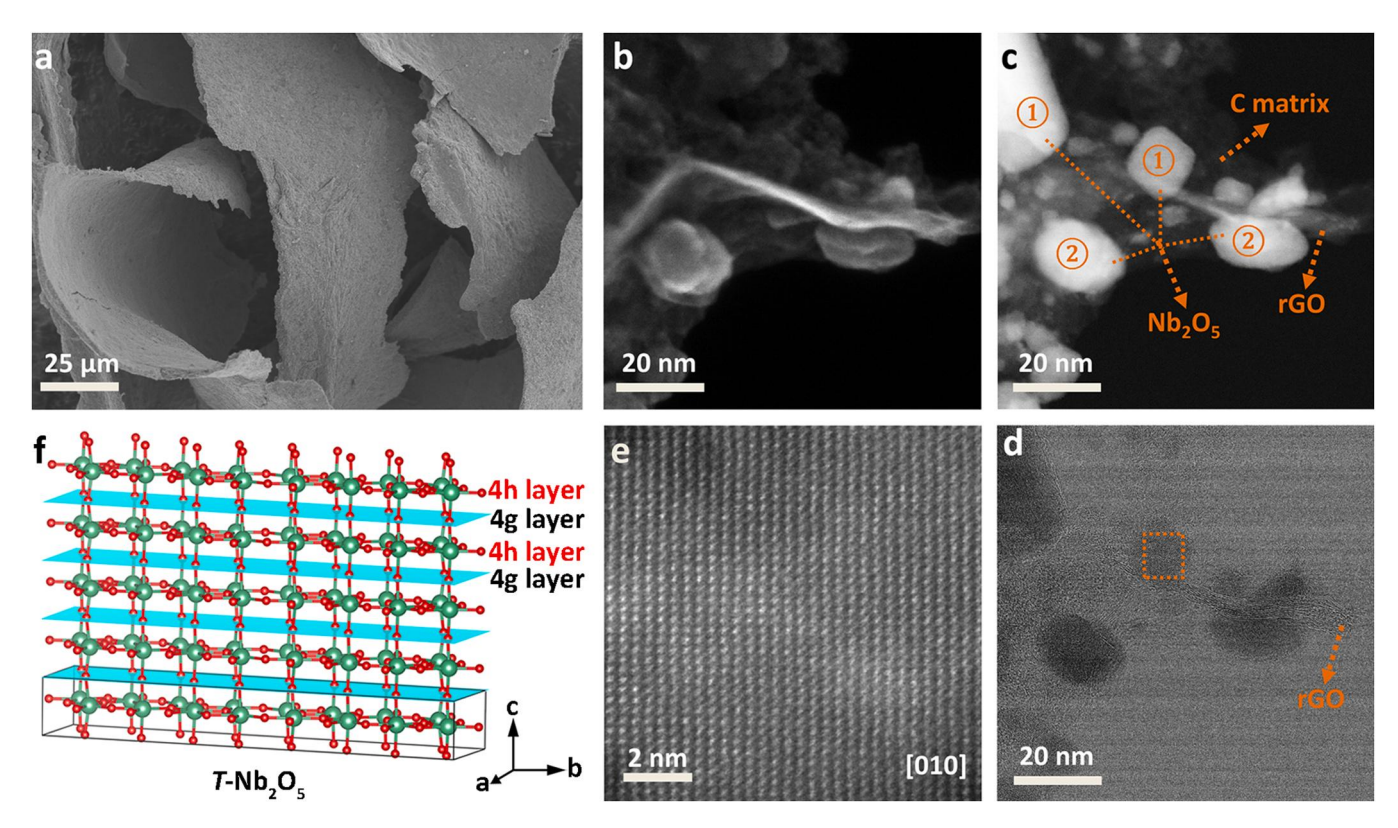


Fig. 2. (a) FE-SEM image, (b–e) STEM images of the as-prepared 2D Nb₂O₅-C-rGO architectures. The mark "1" and "2" in (c) indicates some of Nb₂O₅ nanoparticles are inserted into the carbon matrix while some anchored on the near-surface of the carbon matrix. (f) Part of schematic crystal structure of T-Nb₂O₅, in which green balls are Nb atoms and red balls are O atoms.

comparison with the pure Nb₂O₅ nanoparticles and 2D Nb₂O₅-rGO architecture, it is clear that the bridge-C played a critical role in ensuring good dispersion and suppressing the size of the Nb₂O₅ nanoparticles in the 2D Nb₂O₅-C-rGO architecture. Moreover, the bridge-C is expected to result in improved electron transfer between Nb₂O₅ nanoparticles and rGO. Fig. 2e shows that the Nb₂O₅ particles in 2D Nb₂O₅-C-rGO architecture are highly crystallized with an orthorhombic structure (Tphase). Fig. 2f displays the crystal structure of T-Nb₂O₅, which is alternately composed by 4 h layers of closely packed Nb/O polyhedrons (NbO₆ octahedral and NbO₇ pentagonal bipyramids) and 4 g layers of loosely packed O atoms along z-axis, respectively [19]. Based on the operando Raman spectroscopy and theoretically computational analyses, our previous work proposed that the Li⁺ are likely located at the loosely packed 4 g layers and prefer to form bridge coordination with the O atoms in the densely packed 4 h layers [19]. As a result, the Li ions can directly transfer between the bridging sites with very low steric hindrance [19,33].

The crystallographic phase structures of 2D Nb₂O₅-C-rGO architecture, 2D Nb₂O₅-rGO architecture, Nb₂O₅-C NPs, and Nb₂O₅ NPs were further analyzed using X-ray diffraction (XRD). As presented in Fig. 3a, the XRD patterns of the four samples appear to be similar, which could be assigned to a standard T-Nb₂O₅ (JCPDF: 00-027-1313) without any extra peaks belonging to impurities. The gradually widened full-width at half maximum of peaks from Nb₂O₅ NPs to 2D Nb₂O₅-C-rGO architecture indicates that the $\mathrm{Nb_2O_5}$ grains are getting smaller and smaller. This result is consistent with the results of SEM observation, which can further support that the growth of Nb2O5 grains in 2D Nb2O5-C-rGO architecture were restricted during the synthesis. Fig. 3b shows the Raman spectra of the four materials. All of them present a couple of peaks with similar Raman shifts. The three vibration peaks centered at 694 cm⁻¹, 314 cm⁻¹ and 211 cm⁻¹ can be assigned to Nb-O-Nb bonds of Nb/O polyhedrons in T-Nb₂O₅ [19,27,34]. Compared with the Nb₂O₅ NPs, however, the intensities of these peaks become weaker. Two peaks centered at around 1328 cm⁻¹ and 1602 cm⁻¹ are the D and G-bands of the carbonaceous components for all materials, respectively. It is known that the D-band corresponds to the defect/disordered sp²-hybridized carbon atoms in a two-dimensional hexagonal lattice and the G-band is related to the stretching of C-C bond in graphitic mode of carbon materials [35,36]. The carbon in the Nb₂O₅ NPs might be derived from the oxalate ions $((COO)_2^{2-})$ in the Nb raw materials. The thermogravimetric analysis (TGA) curves displayed in Fig. S3, indicate that the amount of rGO in 2D Nb₂O₅-rGO architecture is 4.11 wt%, the amount of C in Nb₂O₅-C NPs is about 9.62 wt%, the total amount of bridge-C and rGO in the 2D Nb₂O₅-C-rGO architecture is 13.85 wt%. The survey X-ray photoelectron spectroscopy (XPS) spectra of the 2D Nb₂O₅-rGO and 2D Nb₂O₅-rGO architectures and Nb₂O₅ NPs suggests all of them are composited by the targeted Nb, O and C elements (Fig. S4). To learn the detailed chemical states of the Nb and O elements in the surfaces of the three materials, their core-level XPS spectra of Nb3d and O1s are analyzed. The three samples have similar Nb3d XPS spectra (Fig. 3c-e) containing two characteristic peaks of 3d_{1/2} (207.1 eV) and 3d_{3/2} (209.9 eV) due to the strong spin-orbit splitting [20,34]. The fitting results showed that these Nb elements in the those materials are mainly Nb⁵⁺ with minor Nb⁴⁺. It could be attributed to the presence of lattice oxygen vacancies in the Nb₂O₅ as we expected. Compared with 2D Nb₂O₅-rGO architecture, as shown in Table S1, twice as much Nb⁴⁺ is detected in the 2D Nb₂O₅-C-rGO architecture and there are about 2.5 of Nb⁴⁺ in each chemical formula of Nb₁₆O₄₀, which corresponds to a unit cell of Nb₂O₅. In other words, at least one oxygen vacancy is produced in each unit cell of Nb₂O₅. The O1s XPS spectrum shown in Fig. 3f for the pure Nb₂O₅ nanoparticles can also be divided into three peaks. The strongest peak centered at lower binding energy of 530.1 eV can be assigned to the lattice oxygen and the peak centered at the highest binding energy of 533 eV can be attributed to the absorbed hydroxyls or C=O [20]. These peaks are also observed at same positions in the O1s spectra of the 2D Nb₂O₅-rGO (Fig. 3g) and 2D Nb₂O₅-C-rGO

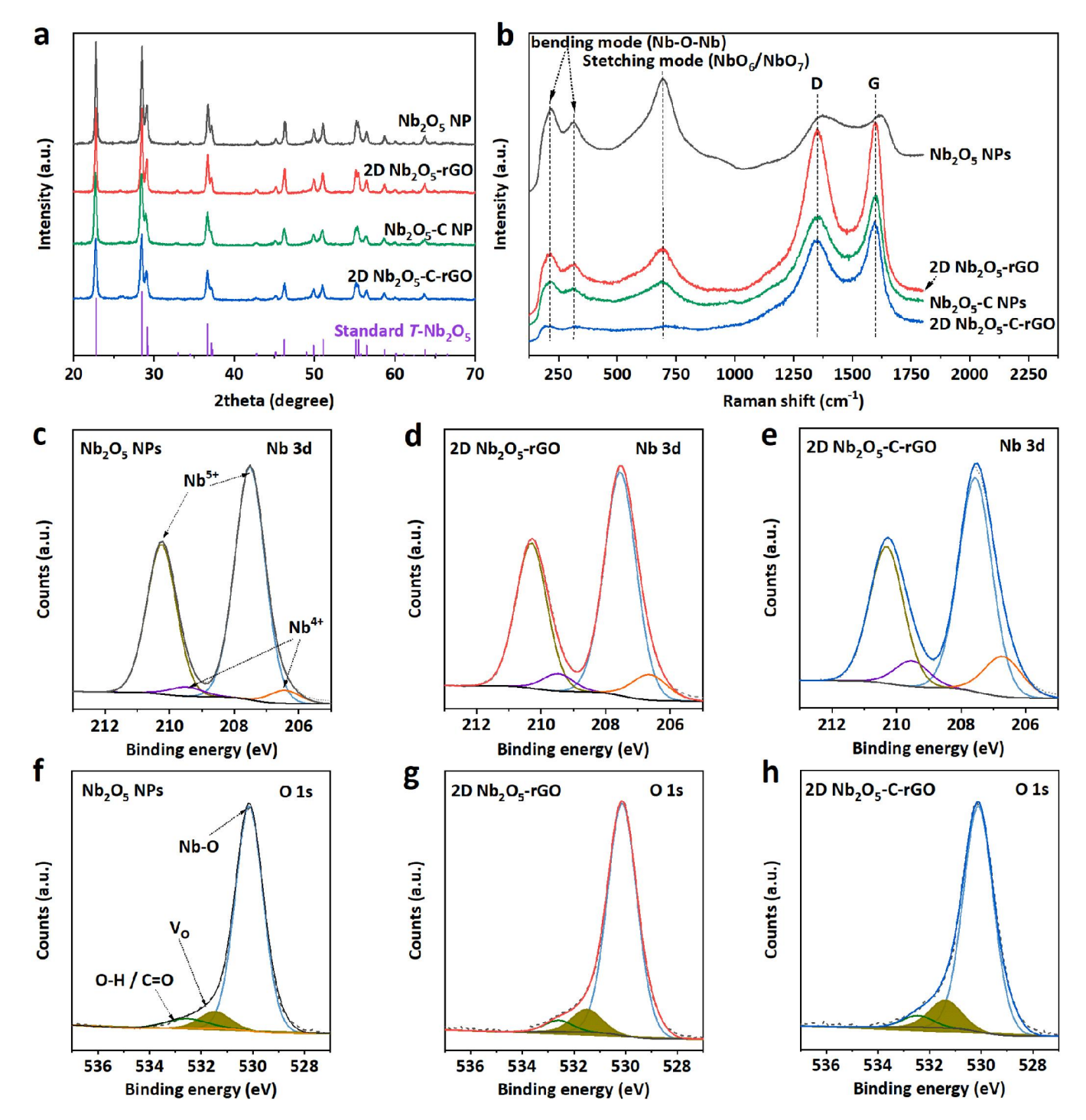


Fig. 3. (a) XRD patterns, (b) Raman spectra, (c–e) Ni 3d and (f-h) O 1s core-level XPS spectra of the Nb_2O_5 NPs, Nb_2O_5 -C NPs, 2D Nb_2O_5 -rGO and Nb_2O_5 -C-rGO architectures.

architectures (Fig. 3h). A weak and broad peak in each spectrum at the binding energy of about 531.7 eV is observed. From literatures, this peak can be assigned to the defect sites with abundant low oxygen coordination, e.g. oxygen vacancy [37,38]. Therefore, the oxygen vacancy-rich 2D Nb₂O₅-C-rGO architecture has been successfully prepared in our case.

The Li⁺ storage capabilities and behaviors of all materials were investigated in coin-cells with metallic Li as the counter electrode. Fig. 4a show the initial cyclic voltammetry (CV) curves recorded at the scan rate of 0.1 mV s⁻¹ in the potential window of 1.0–3.0 V (vs Li⁺/Li) for the Nb₂O₅ NPs, Nb₂O₅-C NPs, 2D Nb₂O₅-rGO and 2D Nb₂O₅-C-rGO

electrode. All the CV curves exhibit a rectangular-like shape in the potential range of 1.0 V ~ 2.25 V with two pairs of redox peaks, consistent with other reported works [20,33], an indication that all anodes present a pseudocapacitive electrochemical behavior. Two pairs of redox peaks were observed for each anode even though there are small differences in the peak positions, as summarized in Table S2. Taking the 2D Nb₂O₅-C-rGO anode as an example, the two reduction peaks were centered at 1.58 V and 1.87 V during discharge, respectively, and the corresponding two oxidation peaks were centered at 1.83 V (broad and strong) and 1.97 V (weak) during charge. These two pairs of peaks are assigned to the Li $^+$ intercalation/de-intercalation in the crystal structure

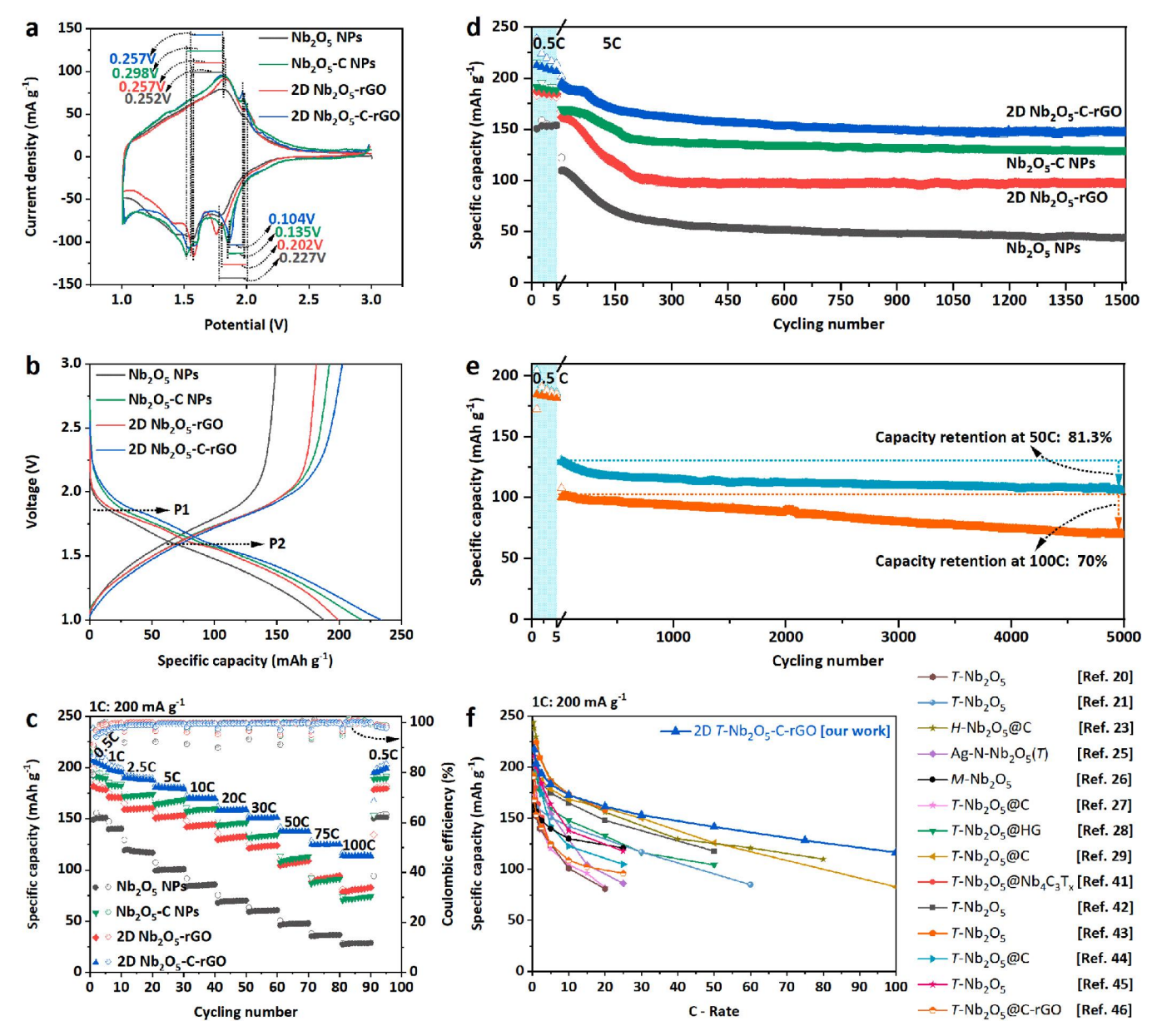


Fig. 4. (a) Initial CV curves, (b) initial discharge-charge profiles, (c) rate capabilities and (d) cycling stabilities at 5 C of pure Nb₂O₅-NPs, Nb₂O₅-C NPs, 2D Nb₂O₅-rGO and 2D Nb₂O₅-C-rGO architectures in the potential range of 1.0–3.0 V. (e) Long-term cycling stability of the 2D Nb₂O₅-C-rGO architectures at 50 C and 100 C in the potential range of 1.1–3.0 V. (f) Rate capability comparison between the 2D Nb₂O₅-C-rGO architecture and other reported Nb₂O₅-based active materials.

of Nb₂O₅ associated with the redox reaction of Nb₂O₅ + xLi^+ + $xe^- \leftrightarrow$ Li_xNb₂O₅, in which x equals 2 for T-Nb₂O₅, corresponding to the Nb^{5+}/Nb^{4+} and Nb^{4+}/Nb^{3+} couples [29,39,40]. Moreover, the 2D Nb₂O₅-C-rGO anode shows the smallest voltage separations (0.26 V and 0.10 V) between the reduction and oxidation peaks, indicating the smallest polarization during the Li⁺ storage process. The initial galvanostatic discharge-charge curves at 0.5 C are shown in Fig. 4b. All four anodes present a smooth potential change with the capacity, suggesting that the Li⁺ storage in the T-Nb₂O₅ is mainly based on the solid-solution reaction without phase transition, which have been proposed and certified by previous works [9,33]. In the discharge curves, two short sloping plateaus marked as P1 and P2 can be observed at average potentials of about 1.56 V and 1.86 V, respectively, which can well coincide with the two reduction peaks in the discharge portion of the CV curves. Among the four anodes, the Nb2O5 NPs delivered the lowest capacity of 188 mAh g⁻¹ with a low coulombic efficiency of 79.2%. All the other three anodes present an enhanced capacity and increased

reversibility. The 2D Nb₂O₅-C-rGO anode delivered the highest discharge specific capacity of 238 mAh g^{-1} and corresponding charge capacity of 206 mAh g⁻¹, which is very close to the theoretical capacity of 200 mAh g^{-1} . The capacity loss in the initial charge-discharge process is due possibly to the irreversible lithium ion reaction with functional groups in the C-rGO framework (Fig. S5), irreversible lithium ion insertion into the distorted sites in the nanosized Nb₂O₅, and/or irreversible formation of solid electrolyte interface (SEI) [23,24]. These irreversible processes contribute to the initial capacity, resulting in higher capacity than the theoretical value (200 mAh g^{-1}) in the first few cycles, which is known as the initial activation process. After the activation process, the capacity contribution from carbon itself was very small (Fig. S5) since the cutoff potential (vs Li/Li⁺) is above 1.0 V. After the 1st cycle, the CV curves and the discharge-charge curves of the subsequent 2nd and 3rd cycles for each anode are almost overlapped (Fig. S6), indicating that all four anodes annealed in N2 have a good stability at the initial stage.

To understand the contribution of oxygen vacancy to the electrochemical performance, the Nb₂O₅ NPs were also prepared by calcination in air for comparison. The specific capacity decreased significantly (Fig. S7b and S7c) in the initial several cycles. The Nb₂O₅ NPs calcined in air exhibited a much worse performance with poor rate capability (73.1 mAh g⁻¹ at 10 C) compared to that of the Nb₂O₅ NPs prepared in N_2 (85.5 mAh g⁻¹ at 10 C). The Nyquist plots (Fig. S7d) indicate that the Nb_2O_5 NPs has a lower resistance by annealing in inert atmosphere (N_2), which is attributed mainly to the presence of a small amount of carbon derived from the Nb5+ salts (Fig. 3b) and oxygen vacancies (Fig. 3c and f). Nevertheless, the enhanced Li⁺ storage performance of the Nb₂O₅ NPs (N₂) is still poor compared to that of the Nb₂O₅-C NPs, 2D Nb₂O₅rGO architecture and 2D Nb₂O₅-C-rGO. Fig. 4c shows the rate performance of each anode and Fig. S8 shows their first discharge-charge curves at different rate. As the rate was increased from 0.5 C (100 mA g^{-1}) to 100 C, the Nb₂O₅ NPs (N₂) anode showed the worst rate performance. In contrast, the Nb₂O₅-C NPs anode (with 9.62 wt% C and average particle size of 57 nm) delivered a higher specific capacity than the 2D Nb₂O₅-rGO anode (with 4% rGO and average particle size of 87 nm) at low rates from 0.5 C to 30 C. As the rate is increased to 30 C and higher, the capacity degradation of the Nb₂O₅-C NPs anode is more serious than that of the 2D Nb₂O₅-rGO anode. Because of the small particle size (33.8 nm) and the efficient 2D C-rGO electronic framework (Fig. S9), the 2D Nb₂O₅-C-rGO anode achieved the highest rate capability among the 4 types of samples. A specific capacity of 114 mA h g^{-1} was achieved at 100 C. As the rate was reduced back to 0.5 C, a specific capacity of 200 mA h g⁻¹ with 100% of the Coulombic efficiency can still be retained. The rate performance achieved by the 2D Nb₂O₅-C-rGO anode is even much higher than that of Nb₂O₅ NPs anode with 20% extra C (Fig. S10), which further confirms the importance of the unique architecture of the 2D Nb₂O₅-C-rGO anode. The rate performance of the 2D Nb₂O₅-C-rGO anode in the potential range of 1.1-3.0 V was also evaluated (Fig. S11). Although the specific capacities delivered at each rates were lower than that delivered in the potential range of 1.0-3.0 V, the capacity difference becomes smaller with increasing the rate. The capacity difference is only $6~\text{mA}~\text{h}~\text{g}^{-1}$ at 50~C. The electrochemical stability of T-Nb₂O₅ could be significantly affected by the potential range. As shown in Fig. 4d, the 2D Nb₂O₅-C-rGO architecture demonstrated a specific capacity of 147 mA h $\rm g^{-1}$ after a long-term testing at $5 \text{ C} (1 \text{ A g}^{-1}) \text{ for } 1500 \text{ cycles in the potential range of } 1.0-3.0 \text{ V}.$ The specific capacity after long-term testing is much higher than that of $Nb_2O_5 NPs$ (43 mAh g^{-1}), Nb_2O_5 -C NPs (129.9 mAh g^{-1}) and $2D Nb_2O_5$ rGO composite architecture (97.4 mAh g^{-1}). Although the corresponding coloumbic efficiencies of the four anodes are above 95%, as presented in Fig. S12, the capacity retentions of 2D Nb₂O₅-C-rGO architecture and Nb₂O₅-C NPs anodes are both about 78%, but that of the Nb₂O₅ NPs and 2D Nb₂O₅-rGO architecture anodes are only 41% and 60%. To further evaluate the long-term cycling stability of the 2D Nb₂O₅-C-rGO architecture, we tested the anode at higher rate of 50 C in the potential ranges of 1.0–3.0 V and 1.1–3.0 V. As shown in Fig. 4e, the anode delivered a stable electrochemical performance (see chargedischarges curves at different cycles in Fig. S13) with a capacity of about 107 mAh g⁻¹ and a retention of 80.12% after 5000 cycles at 50 C in the potential range of 1.1-3.0 V, which is more stable than that obtained at same rate but at lower cut-off potential of 1.0 V (capacity retention: 61.3%) (Fig. S14). Thus, such an excellent Li⁺ storage shows a great potential of the 2D Nb₂O₅-C-rGO architecture for ultrafast lithiumion battery application. As shown in Fig. 4f and Table S3, such a rate capability and cycling stability achieved by the 2D Nb2O5-C-rGO architecture is among the state-of-art Nb₂O₅-based electrodes [20,21,23, 25-29,41-46]. Moreover, the synthesis procedure of the 2D Nb₂O₅-C-rGO architecture is more facile and economical. Besides, the rate capability of the 2D Nb₂O₅-C-rGO architecture depends sensitively on the amount of bridge-C (Fig. S15), which can be controlled by adjusting the amount of DA during the synthesis. Insufficient amount of C may results in poor electronic conductivity while too much may

impede the transport of ${\rm Li}^+$ ions to or from Nb₂O₅ nanoparticles, especially at high rates. Both of the cases can result in a decreased performance.

T-Nb₂O₅ is a well-known intercalation pseudocapacitive anode material. In order to gain insights into the Li⁺ storage mechanism of the 2D Nb₂O₅-C-rGO architecture, we acquired a series of CV measurements at different scan rates. As shown in Fig. 5a, all curves have similar shapes with well-defined redox peaks and with gradually increased enclosed area as the scan rate was varied from 0.1 to 3 mV s⁻¹. According to the relationship of $I_p = a\nu^b$ between the redox peak current (I_p : mA) and the scan rate $(\nu$: mV s⁻¹) of these CV curves, the value of the exponent b usually varies from 0.5 for a diffusion-controlled behavior to 1.0 for a capacitive-controlled behavior, which can be determined from linear fitting of the Log (I) vs. Log (v) profiles based on the power-law of $\log I_{\rm p} =$ $\log a + b \log v$ [27,29,34,47]. As displayed in Fig. 5b, the b values of the 2D Nb₂O₅-C-rGO architecture in anodic and cathodic peaks are calculated to be 0.957 and 0.929, respectively. Therefore, both diffusion-controlled and capacitive-controlled reactions contribute to the Li⁺ storage in the 2D Nb₂O₅-C-rGO architecture. In order to quantify each of their contributions to the total capacity [27,29,34,47], the linear plots of $I(V)/v^{1/2}$ vs. $v^{1/2}$ at different potentials are acquired based on the equation of $I(V) = k_1 v + k_1 v^{1/2}$ (Fig. S16). The derived normalized contribution ratios at different scan rates (Fig. 5c) showed that the Li⁺ storage of the 2D Nb₂O₅-C-rGO architecture at high-rates is dominated mainly by the capacitive-controlled reaction, which increases with increasing scan rate. Moreover, the electrochemical impedance spectroscopy (EIS) and galvanostatic intermittent titration technique (GITT) were used to further characterize the four anodes [47]. Fig. 5d displays the Nyquist plots recorded under the open-circuit voltage; the impedance spectra composed of an inclined line in the low frequency region and a depressed semicircle in the middle-high frequency region, which is generally associated with the charge transfer resistance of the active material [47,48]. The 2D Nb₂O₅-C-rGO architecture exhibits the smallest radius of the semicircle, meaning the lowest charge transfer resistance of the electrode. The fast charge transfer ability can be attributed to its unique microstructure with a well-connected transport network for the electrons (Fig. S9). The GITT data was collected with 5 min current pulse of 0.1 A g^{-1} in the voltage window of 1.0--3 V followed by 0.5 hrelaxation during the Li⁺ insertion and extraction processes of the four

anode materials (Fig. S17). Based on the equation of $D_{\text{Li}} = \,$

$$\frac{4}{\pi\tau} \left(\frac{m_B V_M}{M_B S}\right)^2 \left(\frac{\Delta E_S}{\Delta E_\tau}\right)^2 \ (D_{Li}, \ V_M, \ M_B, \ S, \ \Delta E_S \ and \ \Delta E_\tau \ represents the \ Li^+$$
 diffusion coefficient, molar volume, molar mass, surface area, steady potential difference in the plateau region, voltage drop between during the relaxation of the electrode, respectively, limited time period, m_B represents the quality of active cathode material) [25,33,47] for the GITT curves of potential-time, there is a linear relationship between the D_{Li} and $\left(\frac{\Delta E_S}{\Delta E_\tau}\right)^2$. Since the nanoparticles of the each anode materials are

irregular, it is difficult to obtain a precise diffusion depth (L = $\frac{m_B V_M}{M_B S}$) for each anode. To make a qualitative comparison, the relationships of D_{Li}^*L vs potential for the above four anodes based on their GITT curves can be extracted. As shown in Fig. 5e and f, the 2D Nb₂O₅-C-rGO anode showed the highest Li⁺ diffusion coefficient among the four anodes. Especially, when the potential changed to about 1.85 V and 1.57 V during the discharge (intercalation) process, the Li⁺ diffusion coefficient of 2D Nb₂O₅-C-rGO architecture are nearly 14 and 3.16 times higher than that of the Nb₂O₅ NPs, respectively. During the charge (deintercalation) process, the Li⁺ diffusion coefficient of the Nb₂O₅ NPs dropped very quickly, but that of the 2D Nb₂O₅-C-rGO architecture was more stable. The enhancement of the Li⁺ diffusion of the 2D Nb₂O₅-C-rGO could be attributed to the presence of oxygen vacancies.

In our case, the 2D Nb₂O₅-Carbon-rGO architecture have three

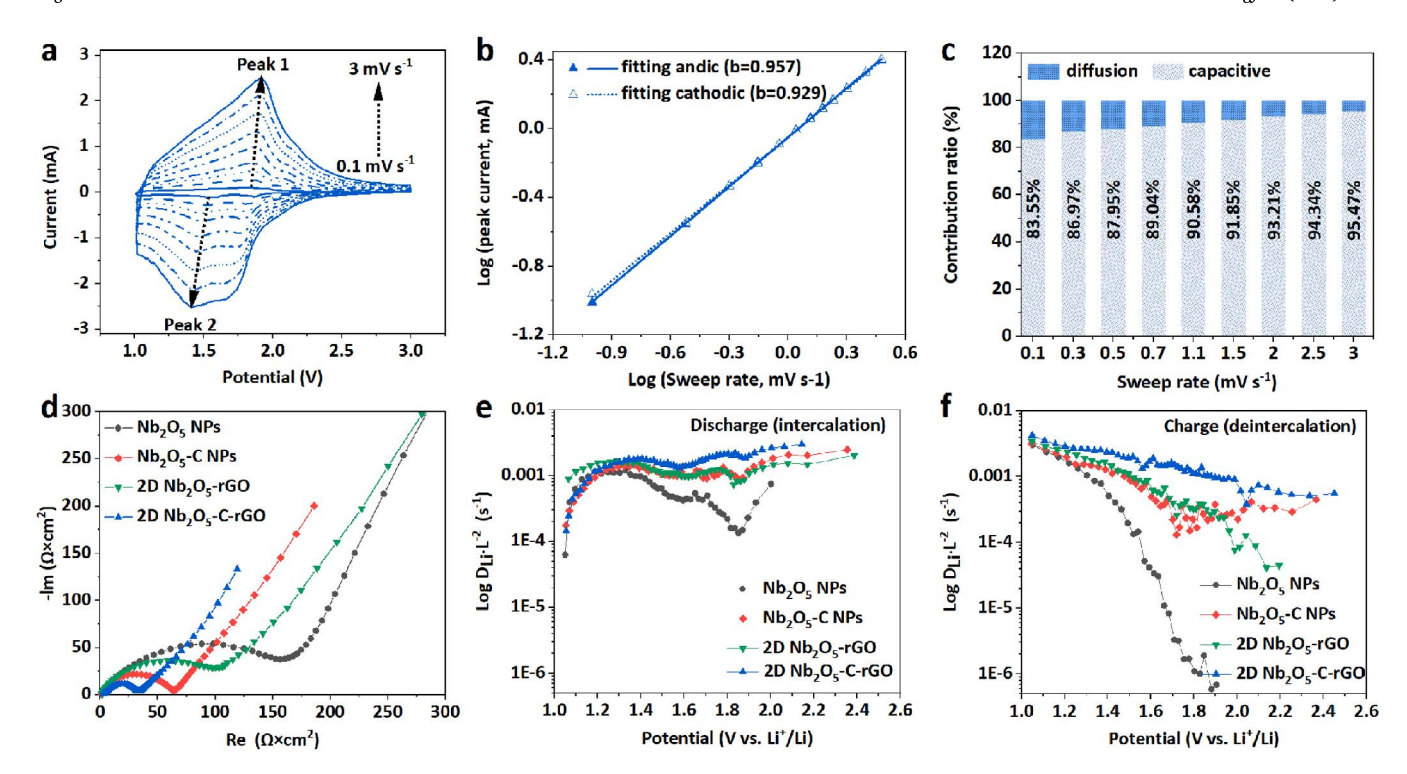


Fig. 5. (a) CV curves, (b) normalized cathodic and anodic peak currents, (c) contribution ratios of capacitive capacities to the total capacities of the 2D Nb₂O₅-C-rGO architecture at various scan rates from 0.1 mV s^{-1} to 3 mV s^{-1} . (d) Nyquist plots and extracted relative diffusion coefficients of Li⁺ during discharge and charge processes from the GITT curves for the pure Nb₂O₅-C NPs, Nb₂O₅-C NPs, 2D Nb₂O₅-rGO and 2D Nb₂O₅-C-rGO architectures.

superiorities including the electronic network of C-rGO, the small grain size of Nb₂O₅, and the considerable numbers of lattice oxygen vacancies, It is believed that the oxygen vacancy also plays a significant role in tuning the electronic and ionic conductivities of the 2D Nb₂O₅-C-rGO architecture. To gain some insight into the effect of oxygen vacancy, we resorted to DFT calculations to examine the electronic and Li⁺ ionic conductivity or diffusion behaviors in the Nb2O5 with and without oxygen vacancy. In the crystal structure of pure T-Nb₂O₅ (Fig. S18), Li⁺ can be compactly and stably adsorbed in the 4 g layer of loosely packed O atoms with a density of $3\text{Li/Nb}_2\text{O}_5$ and adsorption energy of -2.38 eV. Accordingly, Li⁺ can easily move in the 4 g layer. Previous studies show that Li⁺ preferentially transports along the a-axis [19,33] Thus, the electronic structures and Li⁺ transport mechanism along the a-axis in the 4 g layer of defect Nb₂O₅ we systematically examined. The referenced Li⁺ transport pathway for T-Nb₂O₅ in our calculation is proposed by another group [19]. There is at least one oxygen vacancy in a unite cell including 16 Nb and 40 O atoms based on XPS results. Fig. 6a shows the density of state (DOS) of Nb₂O₅ with oxygen vacancy at O1 (VO1 in cyan lines), O2 (VO2 in green lines) and O3 (VO3 in yellow lines) sites along a-axis, respectively, comparing with that of Nb₂O₅ with no oxygen vacancy. The corresponded positions are shown in the top view from the c axis below the DOS plots. The results showed that both the valance Nb d bands (solid lines) and O p bands (dashed lines) shift to higher energy due mainly to the electron deficiency induced from the oxygen vacancy formation. Additionally, Nb d bands can form small spikes slightly above the Fermi level for those defect Nb₂O₅, contributing mainly from those Nb neighboring to the vacancy. Therefore, oxygen vacancy induces higher energetic shift of O p bands and the additional distribution around the Fermi level of Nb d bands, and then narrows the band-gap and enhances the electronic conductivity. Moreover, it is notice that the bridge-C adsorbed on the surface of Nb₂O₅ particle in the 3D architecture can also reduce the band-gap and improve electronic conductivity of Nb₂O₅ (Fig. S19). In details, the surface bridge-carbon of Nb₂O₅ particles can induce the extra distribution of Nb d band in the Fermi level, although it shifts valance Nb d band and oxygen p band to lower energy (opposite to the oxygen vacancy). Then, the DOS analysis shows that the enhanced electronic conductivity obtained on 2D Nb₂O₅-C-rGO can still be attributed to the altered Nb d band structure with a small distribution around the Fermi level, induced by both the oxygen vacancy and bridge-carbon thin layer on the surface of Nb₂O₅. Besides the altered electronic structure, oxygen vacancy can also change the adsorption behavior of Li⁺ on defect Nb₂O₅. Fig. 6b compares the adsorption energies of Li⁺ (E_{ads}) on O1–O3 sites of Nb₂O₅ without (O_O in red bars) and with oxygen vacancies of V_{O1} (cyan bars), V_{O2} (green bars) and V_{O3} (yellow bars). The detailed adsorption structures on perfect Nb₂O₅, for example, are shown in the top views below. The comparison result finds that the Li⁺ has weaker E_{ads} on defect Nb₂O₅ because of the repulsion between positively charged vacancy site and Li⁺. Among the three sites of the defect Nb₂O₅, Li⁺ has the weakest E_{ads} when adsorbing on O2 site with oxygen vacancy (V_{O2}) . As shown in Fig. 6c, the oxygen vacancy induced weaker E_{ads} alters the energy profile for Li⁺ transport along the a-axis. The overall barrier difference between the highest and lowest energies along the whole profile for Li⁺ diffusion is reduced on the defect Nb_2O_5 (0.57–0.62 eV) from the prefect Nb_2O_5 (0.74 eV). As a result, oxygen vacancy induced weaker Eads can effectively reduce the diffusion barrier and enhance Li⁺ ionic conductivity for the better electrochemical performance. Additionally, the weaker Eads or repulsion between oxygen vacancy and Li⁺ can be further utilized to improve the diffusion kinetics by directing Li⁺ diffusion pathway with aligned the vacancy.

3. Conclusion

In summary, a 2D T-Nb₂O₅-C-rGO architecture was successfully designed to achieve enhanced Li⁺ storage performance for fast-rechargeable LIBs. When tested as an anode in an LIB, the 2D Nb₂O₅-C-rGO architecture shows attractive rate performance with a specific capacity of 114 mAh g⁻¹ at 100 C and stable long-term cycling performance with a capacity of 147 mAh g⁻¹ delivered at 5 C after 1,150 cycles and 107 mAh g⁻¹ obtained at 50 C after 5,000 cycles. As confirmed

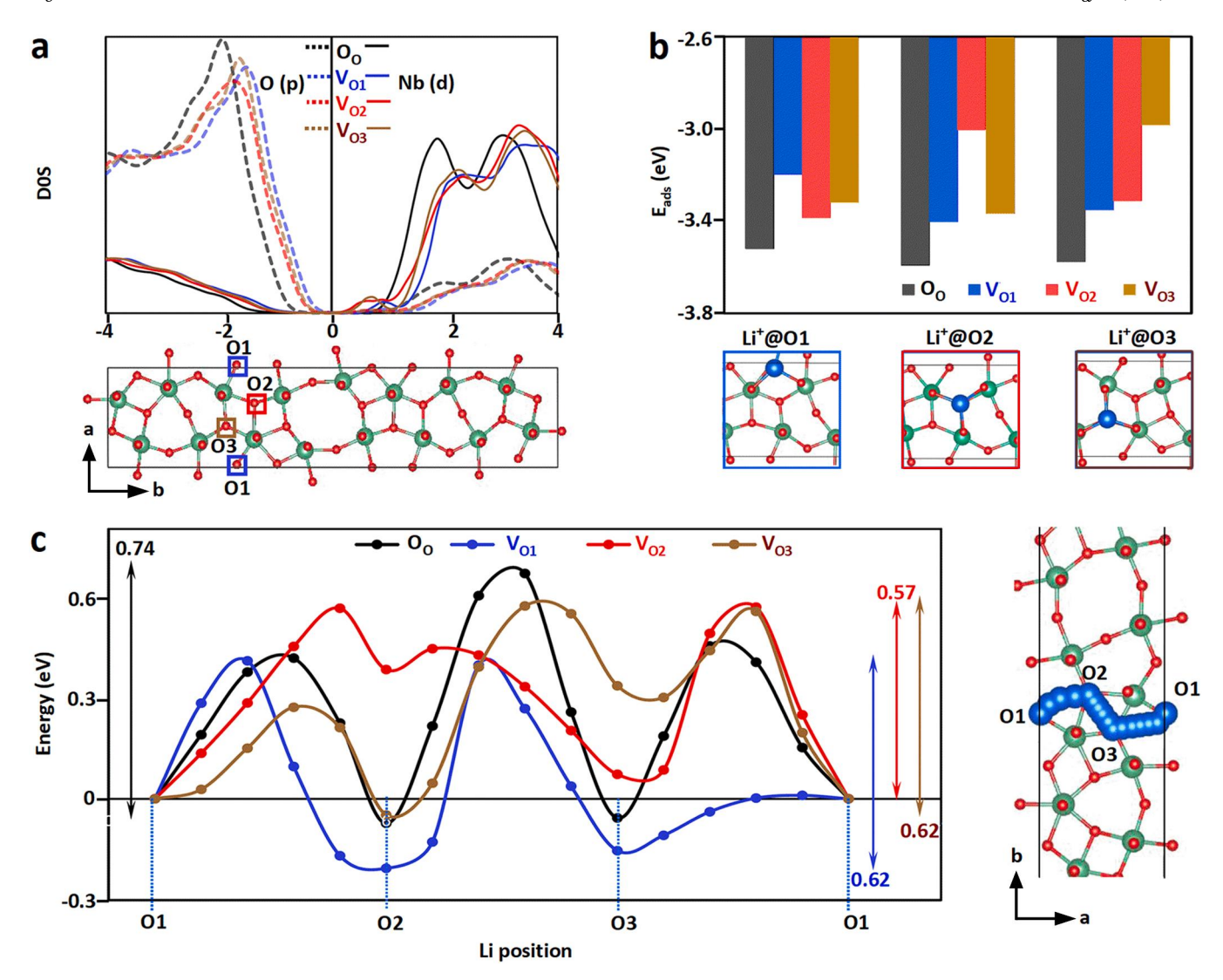


Fig. 6. (a) DOS analysis of defect Nb₂O₅ with oxygen vacancy at O1 (V_{O1} in cyan lines), O2 (V_{O2} in green lines) and O3 (V_{O3} in yellow lines), comparing with that for perfect Nb₂O₅ (O_{O} in red lines). Corresponded positions are shown in the top view from the c axis in the below. Valance Nb d bands and O p bands are represented in solid and dashed lines, respectively. (b) Bar chart for the E_{ads} of Li ion at O1, O2 and O3 sites on prefect (O_{O} , red bars) and defect Nb₂O₅ of V_{O1} , V_{O2} and V_{O3} in cyan, green and yellow bars, respectively. Corresponded structures for the adsorptions on perfect Nb₂O₅, for example, are shown below. (c) Energy profile of Li diffusion along the a-axis (O1 \leftrightarrow O2 \leftrightarrow O3 \leftrightarrow O1). Corresponded structure for the diffusion is shown in the right.

by detailed experimental and computational investigations, the excellent ${\rm Li}^+$ storage performance of the 2D Nb₂O₅-C-rGO architecture is attributed to the enhanced electronic conductivity of the electrode (resulted from the in-situ formed bridge-C to optimize the electronic network of rGO and lower the band-gap) and to fast ${\rm Li}^+$ diffusion in the bulk phase of Nb₂O₅ (resulted from the in-situ formed lattice oxygen vacancy to alter the Nb d band structure and lower the diffusion barrier of ${\rm Li}^+$).

CRediT authorship contribution statement

Panpan Jing: Investigation, Methodology, Data curation, Writing – original draft. Kuanting Liu: Computation, Analysis. Luke Soule: Data curation, Writing-Editing. Jeng-Han Wang: Computation, Software, Writing-Reviewing. Tongtong Li: Data curation. Bote Zhao: Visualization, Analysis, Writing – review & editing. Meilin Liu: Supervision, Resources, Conceptualization, Visualization, Writing-Reviewing.

Declaration of Competing Interest

The authors declare that they have no known competing financial

interests or personal relationships that could have appeared to influence the work reported in this paper.

Acknowledgements

This work was supported by CBMM, US National Science Foundation (DMR-1742828), and the National Natural Science Foundation of China (51702201). P. J. acknowledges the financial support of a scholarship from the China Scholarship Council (CSC).

Appendix A. Supporting information

Supplementary data associated with this article can be found in the online version at doi:10.1016/j.nanoen.2021.106398.

References

- [1] Z.P. Cano, D. Banham, S. Ye, A. Hintennach, J. Lu, M. Fowler, Z. Chen, Batteries and fuel cells for emerging electric vehicle markets, Nat. Energy 3 (2018) 279–289.
- [2] X. Zeng, M. Li, D. Abd El-Hady, W. Alshitari, A.S. Al-Bogami, J. Lu, K. Amine, Commercialization of Lithium Battery Technologies for Electric Vehicles, Adv. Energy Mater. 9 (2019), 1900161.

- [3] Y. Liu, Y. Zhu, Y. Cui, Challenges and opportunities towards fast-charging battery materials, Nat. Energy 4 (2019) 540–550.
- [4] B. Zhao, R. Ran, M. Liu, Z. Shao, A comprehensive review of Li₄Ti₅O₁₂ -based electrodes for lithium-ion batteries: the latest advancements and future perspectives, Mater. Sci. Eng. R Rep. 98 (2015) 1–71.
- [5] Q. Fan, H.-J. Noh, Z. Wei, J. Zhang, X. Lian, J. Ma, S.-M. Jung, I.-Y. Jeon, J. Xu, J.-B. Baek, Edge-thionic acid-functionalized graphene nanoplatelets as anode materials for high-rate lithium ion batteries, Nano Energy 62 (2019) 419–425.
- [6] Z. Pan, H. Sun, J. Pan, J. Zhang, B. Wang, H. Peng, The creation of hollow walls in carbon nanotubes for high-performance lithium ion batteries, Carbon 133 (2018) 384–389.
- [7] Q. Ni, R. Dong, Y. Bai, Z. Wang, H. Ren, S. Sean, F. Wu, H. Xu, C. Wu, Superior sodium-storage behavior of flexible anatase TiO₂ promoted by oxygen vacancies, Energy Storage Mater. 25 (2020) 903–911.
- [8] T. Yuan, Z. Tan, C. Ma, J. Yang, Z.-F. Ma, S. Zheng, Challenges of spinel Li₄Ti₅O₁₂ for lithium-ion battery industrial applications, Adv. Energy Mater. 7 (2017), 1601625
- [9] V. Augustyn, J. Come, M.A. Lowe, J.W. Kim, P.L. Taberna, S.H. Tolbert, H. D. Abruna, P. Simon, B. Dunn, High-rate electrochemical energy storage through Li + intercalation pseudocapacitance, Nat. Mater. 12 (2013) 518–522.
- [10] Q. Fan, L. Lei, Y. Sun, Facile synthesis of a 3D-porous LiNbO₃ nanocomposite as a novel electrode material for lithium ion batteries, Nanoscale 6 (2014) 7188–7192.
- [11] L. Hu, L. Luo, L. Tang, C. Lin, R. Li, Y. Chen, Ti₂Nb_{2x}O₄₊₅ xanode materials for lithium-ion batteries: a comprehensive review, J. Mater. Chem. A 6 (2018) 9799–9815.
- [12] K.J. Griffith, K.M. Wiaderek, G. Cibin, L.E. Marbella, C.P. Grey, Niobium tungsten oxides for high-rate lithium-ion energy storage, Nature 559 (2018) 556–563.
- [13] Q. Zhang, H. Chen, L. Luo, B. Zhao, H. Luo, X. Han, J. Wang, C. Wang, Y. Yang, T. Zhu, M. Liu, Harnessing the concurrent reaction dynamics in active Si and Ge to achieve high performance lithium-ion batteries, Energy Environ. Sci. 11 (2018) 669–681.
- [14] L. Chen, G. Zhou, Z. Liu, X. Ma, J. Chen, Z. Zhang, X. Ma, F. Li, H.-M. Cheng, W. Ren, Scalable Clean exfoliation of high-quality few-layer black phosphorus for a flexible lithium ion battery, Adv. Mater. 28 (2016) 510–517.
- [15] W. Li, X. Sun, Y. Yu, Si-, Ge-, Sn-based anode materials for lithium-ion batteries: from structure design to electrochemical performance, Small Methods 1 (2017), 1600037.
- [16] P. Jing, P. Wang, M. Liu, W. Gao, Y. Cui, Z. Wang, Y. Pu, J. Alloy. Compd. 774 (2019) 236–243.
- [17] P. Geng, S. Zheng, H. Tang, R. Zhu, L. Zhang, S. Cao, H. Xue, H. Pang, Transition Metal sulfides based on graphene for electrochemical energy storage, Adv. Energy Mater. 8 (2018), 1703259.
- [18] Z. Luo, J. Zhou, L. Wang, G. Fang, A. Pan, S. Liang, Two-dimensional hybrid nanosheets of few layered MoSe₂ on reduced graphene oxide as anodes for longcycle-life lithium-ion batteries. J. Mater. Chem. A 4 (2016) 15302–15308.
- [19] D. Chen, J.H. Wang, T.F. Chou, B. Zhao, M.A. El-Sayed, M. Liu, J. Am, Unraveling the nature of anomalously fast energy storage in T-Nb₂O₅, J. Am. Chem. Soc. 139 (2017) 7071–7081.
- [20] S. Shen, S. Zhang, X. Cao, S. Deng, G. Pan, Q. Liu, X. Wang, X. Xia, J. Tu, Energy Storage Mater. 25 (2020) 695–701.
- [21] K.J. Griffith, A.C. Forse, J.M. Griffin, C.P. Grey, High-rate intercalation without nanostructuring in metastable Nb₂O₅ bronze phases, J. Am. Chem. Soc. 138 (2016) 8888–8899.
- [22] Y. Yang, J. Zhao, Wadsley–Roth crystallographic shear structure niobium-based oxides: promising anode materials for high-safety lithium-ion batteries, Adv. Sci. 8 (2021), 2004855.
- [23] Z. Song, H. Li, W. Liu, H. Zhang, J. Yan, Y. Tang, J. Huang, H. Zhang, X. Li, Ultrafast and stable Li-(De) intercalation in a large single crystal H-Nb₂O₅ Anode via optimizing the homogeneity of electron and ion transport, Adv. Mater. 32 (2020), 2001001.
- [24] F. Shen, Z. Sun, Q. He, J. Sun, R.B. Kaner, Y. Shao, Mater. Horiz. 8 (2021) 1130–1152.
- [25] J.Y. Cheong, C. Kim, J.-W. Jung, K.R. Yoon, S.-H. Cho, D.-Y. Youn, H.-Y. Jang, I.-D. Kim, Formation of a surficial bifunctional nanolayer on Nb_2O_5 for ultrastable electrodes for lithium-ion battery, Small 13 (2017), 1603610.
- [26] Z. Hu, Q. He, Z. Liu, X. Liu, M. Qin, B. Wen, W. Shi, Y. Zhao, Q. Li, L. Mai, Science Bull 65 (2020) 1154–1162.
- [27] E. Lim, C. Jo, H. Kim, M.-H. Kim, Y. Mun, J. Chun, Y. Ye, J. Hwang, K.-S. Ha, K. C. Roh, K. Kang, S. Yoon, J. Lee, Facile synthesis of Nb₂O₅@carbon core-shell nanocrystals with controlled crystalline structure for high-power anodes in hybrid supercapacitors, ACS Nano 9 (2015) 7497–7505.
- [28] H. Sun, L. Mei, J. Liang, Z. Zhao, C. Lee, H. Fei, M. Ding, J. Lau, M. Li, C. Wang, X. Xu, G. Hao, B. Papandrea, I. Shakir, B. Dunn, Y. Huang, X. Duan, Three-dimensional holey-graphene/niobia composite architectures for ultrahigh-rate energy storage, Science 356 (2017) 599–604.
- [29] X. Han, P.A. Russo, N. Goubard-Bretesché, S. Patanè, S. Santangelo, R. Zhang, N. Pinna, Exploiting the condensation reactions of acetophenone to engineer carbon-encapsulated Nb₂O₅ nanocrystals for high-performance Li and Na energy storage systems, Adv. Energy Mater. 9 (2019), 1902813.
- [30] S. Deng, Y. Zhang, D. Xie, L. Yang, G. Wang, X. Zheng, J. Zhu, X. Wang, Y. Yu, G. Pan, X. Xia, J. Tu, Nano Energy 58 (2019) 355–364.
- [31] W. Zhang, L. Cai, S. Cao, L. Qiao, Y. Zeng, Z. Zhu, Z. Lv, H. Xia, L. Zhong, H. Zhang, X. Ge, J. Wei, S. Xi, Y. Du, S. Li, X. Chen, Interfacial lattice-strain-driven generation of oxygen vacancies in an aerobic-annealed TiO₂(B) electrode, Adv. Mater. 31 (2019), 1906156.

- [32] T. Yuan, S. Luo, L. Soule, J.-H. Wang, Y. Wang, D. Sun, B. Zhao, W. Li, J. Yang, S. Zheng, M. Liu, Mater. Today (2021).
- [33] J. Meng, Q. He, L. Xu, X. Zhang, F. Liu, X. Wang, Q. Li, X. Xu, G. Zhang, C. Niu, Z. Xiao, Z. Liu, Z. Zhu, Y. Zhao, L. Mai, Identification of phase control of carbon-confined Nb₂O₅ nanoparticles toward high-performance lithium storage, Adv. Energy Mater. 9 (2019), 1802695.
- [34] S. Hemmati, G. Li, X. Wang, Y. Ding, Y. Pei, A. Yu, Z. Chen, 3D N-doped hybrid architectures assembled from 0D T-Nb₂O₅ embedded in carbon microtubes toward high-rate Li-ion capacitors, Nano Energy 56 (2019) 118–126.
- [35] Y. Zhang, Q. Ma, S. Wang, X. Liu, L. Li, Poly(vinyl alcohol)-assisted fabrication of hollow carbon spheres/reduced graphene oxide nanocomposites for highperformance lithium-ion battery anodes, ACS Nano 12 (2018) 4824–4834.
- [36] T. Hoshide, Y. Zheng, J. Hou, Z. Wang, Q. Li, Z. Zhao, R. Ma, T. Sasaki, F. Geng, Flexible lithium-ion fiber battery by the regular stacking of two-dimensional titanium oxide nanosheets hybridized with reduced graphene oxide, Nano Lett. 17 (2017) 3543–3549.
- [37] H. Yuan, J. Li, W. Yang, Z. Zhuang, Y. Zhao, L. He, L. Xu, X. Liao, R. Zhu, L. Mai, Oxygen vacancy-determined highly efficient oxygen reduction in NiCo₂O₄/hollow carbon spheres, ACS Appl. Mater. Interfaces 10 (2018) 16410–16417.
- [38] B. Liu, C. Li, G. Zhang, X. Yao, S.S.C. Chuang, Z. Li, Oxygen Vacancy promoting dimethyl carbonate synthesis from CO₂ and methanol over Zr-doped CeO₂ nanorods, ACS Catal. 8 (2018) 10446–10456.
- [39] S. Lou, X. Cheng, L. Wang, J. Gao, Q. Li, Y. Ma, Y. Gao, P. Zuo, C. Du, G. Yin, High-rate capability of three-dimensionally ordered macroporous T-Nb2O5 through Li+intercalation pseudocapacitance, J. Power Sources 361 (2017) 80–86.
- [40] Y. Jiao, H. Zhang, H. Zhang, A. Liu, Y. Liu, S. Zhang, Highly bonded T-Nb₂O₅/rGO nanohybrids for 4 V quasi-solid state asymmetric supercapacitors with improved electrochemical performance, Nano Res. 11 (2018) 4673–4685.
- [41] C. Zhang, S.J. Kim, M. Ghidiu, M.-Q. Zhao, M.W. Barsoum, V. Nicolosi, Y. Gogotsi, Layered Orthorhombic Nb₂O₅@Nb₄C₃T_x and TiO₂@Ti₃C₂T_x hierarchical composites for high performance Li-ion batteries, Adv. Funct. Mater. 26 (2016) 4143–4151.
- [42] R. Bi, N. Xu, H. Ren, N. Yang, Y. Sun, A. Cao, R. Yu, D. Wang, A hollow multishelled structure for charge transport and active sites in lithium-ion capacitors, Angew. Chem. Int. Ed. Engl. 59 (2020) 4865–4868.
- [43] B. Deng, T. Lei, W. Zhu, L. Xiao, J. Liu, In-plane assembled orthorhombic Nb₂O₅ nanorod films with high-rate Li+ intercalation for high-performance flexible Li-ion capacitors, Adv. Funct. Mater. 28 (2018), 1704330.
- [44] S. Liu, J. Zhou, Z. Cai, G. Fang, Y. Cai, A. Pan, S. Liang, Nb₂O₅ quantum dots embedded in MOF derived nitrogen-doped porous carbon for advanced hybrid supercapacitor applications, J. Mater. Chem. A 4 (2016) 17838–17847.
- [45] S. Fu, Q. Yu, Z. Liu, P. Hu, Q. Chen, S. Feng, L. Mai, L. Zhou, Yolk–shell Nb₂O₅ microspheres as intercalation pseudocapacitive anode materials for high-energy Liion capacitors, J. Mater. Chem. A 7 (2019) 11234–11240.
- [46] X. Jiao, Q. Hao, X. Xia, Z. Wu, W. Lei, Metal organic framework derived Nb₂O₅@C nanoparticles grown on reduced graphene oxide for high-energy lithium ion capacitors, Chem. Commun. 55 (2019) 2692–2695.
- [47] X. Yang, A.L. Rogach, Electrochemical techniques in battery research: a tutorial for nonelectrochemists, Adv. Energy Mater. 9 (2019), 1900747.
- [48] A.R.C. Bredar, A.L. Chown, A.R. Burton, B.H. Farnum, Electrochemical impedance spectroscopy of metal oxide electrodes for energy applications, ACS Appl. Energy Mater. 3 (2020) 66–98.



Panpan Jing is the associate professor in School of Materials Science and Engineering at Shaanxi University of Science and Technology, Xi'an, China. He received his Ph.D. from Lanzhou University in 2016. he is currently working as a visiting research faculty under the supervision of Prof. Meilin Liu in Georgia Institute of Technology, Atlanta, USA. His research interests are focused on developing materials and fundamental mechanism studies for electrochemical energy storage devices, dielectric energy storage devices and photocatalysis.



Guan-Ting Liu is currently the M.S. student of Chemistry Department at National Taiwan Normal University. He received her B.S. degree from National Taiwan Normal University in 2013. His current research focused on density functional theory calculation to investigate the mechanisms of ion transportation of Lithium-ion battery, methanol oxidation reaction and hydrogen evolution reaction on novel catalysts.



Luke Soule is a Ph.D. student at the Georgia Institute of Technology studying under Dr. Meilin Liu. Luke's research interests focus on developing and understanding inorganic and organic chemistries to achieve desired outcomes in energy storage systems. His work pays particular attention to engineering material systems based on fundamental understanding of their electrochemical properties.



Bote Zhao is currently a professor at School of Environment and Energy in South China University of Technology, China. He was a research scientist at the School of Materials Science and Engineering at Georgia Institute of Technology, USA. He received his B.S. and Ph.D. from Nanjing Tech University, China, and continued his career as a postdoctoral fellow at Georgia Institute of Technology, USA. His research interests include the rational design, synthesis and in-situ/operando characterization of advanced materials for efficient energy storage and conversion.



Jeng-Han Wang is the professor of Chemistry Department at National Taiwan Normal University. He received his B.S. and M.S. from National Taiwan University and Ph.D. in Chemistry from Emory University. He then worked as a postdoctoral fellow in the School of Materials Science and Engineering at Georgia Institute of Technology. His research utilizes the quantum mechanical calculation and simulation to investigate mechanisms of important catalytic reactions and reveal intrinsic characters of advanced functional materials in the applications of rechargeable batteries, fuel cells, electrochemical devices and spintronics.



Meilin Liu is the Hightower Chair, Regents' Professor, and Associate Chair for Academics of School of Materials Science and Engineering at Georgia Institute of Technology, Atlanta, Georgia, USA. He received his BS from South China University of Technology and both M.S. and Ph.D. from University of California at Berkeley. His research interests include design, fabrication, in situ/operando characterization, and modeling of membranes, thin films, and nanostructured electrodes in devices for energy storage and conversion, aiming at achieving rational design of materials and structures with unique functionalists.



Tongtong Li received his B.S. in 2014 from Applied Chemistry in Northeastern University, China. He is now pursuing his Ph. D. degree at Northeastern University, China. he worked as a visiting student in Prof. Meilin Liu's group at Georgia Institute of Technology from 2018 to 2021. His research interests are mainly focused on the preparation and characterization of novel materials for energy storage and conversion.